A new mass and radius determination of the ultra-short period planet K2-106b and the fluffy planet K2-106c

Monthly Notices of the ROYAL ASTRONOMICAL SOCIETY

MNRAS **529,** 141–154 (2024) https://doi.org/10.1093/mnras/stae494
Advance Access publication 2024 February 21

A new mass and radius determination of the ultra-short period planet K2-106b and the fluffy planet K2-106c

E. W. Guenther [1]★ E. Goffo,[1,2] D. Sebastian [3] A. M. S. Smith [4] C. M. Persson,[5] M. Fridlund [5,6] D. Gandolfi [2] and J. Korth[7]

[1]*Thüringer Landesternwarte Tautenburg, Sternwarte 5, D-07778 Tautenburg, Germany*
[2]*Dipartimento di Fisica, Universita degli Studi di Torino, via Pietro Giuria 1, I-10125 Torino, Italy*
[3]*School of Physics and Astronomy University of Birmingham, Birmingham University, Edgbaston Park Rd, Birmingham B15 2TT, UK*
[4]*Institute of Planetary Research, German Aerospace Center (DLR), Rutherfordstrasse 2, D-12489 Berlin,, D-12489 Berlin, Germany*
[5]*Department of Space, Earth and Environment, Chalmers University of Technology, Onsala Space Observatory, SE-439 92 Onsala, Sweden*
[6]*Leiden Observatory, University of Leiden, PO Box 9513, NL-2300 RA Leiden, the Netherlands*
[7]*Lund Observatory, Division of Astrophysics, Department of Physics, Lund University, Box 118, SE-22100 Lund, Sweden*

Accepted 2024 February 14. Received 2024 February 13; in original form 2023 January 20

ABSTRACT

Ultra-short period planets (USPs) have orbital periods of less than 1 d. Since their masses and radii can be determined to a higher precision than long-period planets, they are the preferred targets to determine the density of planets which constrains their composition. The K2-106 system is particularly interesting because it contains two planets of nearly identical masses. One is a high-density USP, the other is a low-density planet that has an orbital period of 13 d. Combining the *Gaia* DR3 results with new ESPRESSO data allows us to determine the masses and radii of the two planets more precisely than before. We find that the USP K2-106 b has a density consistent with an Earth-like composition, and K2-106 c is a low-density planet that presumably has an extended atmosphere. We measure a radius of $R_p = 1.676^{+0.037}_{-0.037}$ $R_\oplus$, a mass of $M_p = 7.80^{+0.71}_{-0.70}$ $M_\oplus$, and a density of $\rho = 9.09^{+0.98}_{-0.98}$ g cm^{-3} for K2-106 b. For K2-106 c, we derive $R_p = 2.84^{+0.10}_{-0.08}$ $R_\oplus$, $M_p = 7.3^{+2.5}_{-2.4}$ $M_\oplus$, and a density of $\rho = 1.72^{+0.66}_{-0.58}$ g cm^{-3}. We finally discuss the possible structures of the two planets with respect to other low-mass planets.

Key words: planets and satellites: fundamental parameters – planets and satellites: individual: K2-106b and K2-106c – planets and satellites: interiors – stars: fundamental parameters – stars: late-type.

1 INTRODUCTION

Ultra-short period planets (USPs) are an enigmatic subset of exoplanets with orbital periods less than 1 d. USPs are the focus of many research programs because their masses and radii can easily be determined with high precision. This stems from large radial velocity (RV) amplitudes and easy detection of a large number of transits. The first USP, and the first rocky exoplanet discovered, was CoRoT-7 b (Léger et al. 2009).

Low-mass USPs (lmUSPs) are particularly interesting to study, because they cannot have extended hydrogen atmospheres. This is because any hydrogen atmosphere would be quickly eroded by X-ray and extreme UV radiation from the host star (Fossati et al. 2017; Kubyshkina et al. 2018). They are thus often referred to as bare rocks. Measurements of their densities thus allow us to draw conclusions about the internal structure of rocky planets. Planets without an H/He atmosphere can have masses up to 25 $M_\oplus$ (Otegi, Bouchy & Helled 2020). We therefore define lmUSPs as planets with $P_{orb} < 1$ d, and $Mp < 25M_\oplus$. Currently 35 USPs have been discovered in the mass range between 1 and 25 $M_\oplus$.

Another reason to study lmUSPs is that their formation is still being debated with several possible scenarios (Uzsoy, Rogers & Price 2021). One scenario is that lmUSPs are the remnant cores of gas-giants that lost their atmospheres due to photoevaporation, or Roche-lobe overflow (Mocquet, Grasset & Sotin 2014; Armstrong et al. 2020). TOI-849 b has been suggested to be a remnant of a gas giant, because it has as mass of $39.1^{+2.7}_{-2.6}$ $M_\oplus$, and a density of $\rho = 5.2^{+0.7}_{-0.8}$ g cm^{-3} (Armstrong et al. 2020). However, not all gas-giant USPs evaporate, as has been shown by the discoveries of WASP-18b (Hellier et al. 2009), WASP-19b (Hebb et al. 2010), and NGTS-10b (McCormac et al. 2020).

A second scenario is that lmUSPs have developed through mass accretion in the innermost part of the protoplanetary disc (Petrovich, Deibert & Wu 2019). Because lmUSPs should be bare rocks, one would expect that they should all have densities consistent with the abundances of rock-forming elements of their host stars. However that is not the case; it looks like that lmUSPs are more diverse. The theoretical mass–radius relation has recently been derived for rocky and for volatile rich planets by Otegi et al. (2020).

We can define three classes of low-mass planets:

(i) Planets with densities that are lower than that of a planet with Earth-like core-to-mantle ratio.

★ E-mail: guenther@tls-tautenburg.de

(ii) Planets whose density is consistent with an Earth-like core-to-mantle ratio.

(iii) Planets with densities that are higher than for a planet with an Earth-like core-to-mantle ratio.

Given that the composition of planets is only inferred from the density measurement, we prefer to classify the planets based only on their density, rather than their inferred composition.

Gas-giant USPs fall into class-A but WASP-18b, WASP-19b, and NGTS-10b have more than $25M_{\oplus}$, and are thus not lmUSPs. Examples for class-A lmUSPs are 55 Cnc e (Crida et al. 2018), and WASP-47 e (Vanderburg et al. 2017). They can also have masses below $2M_{\oplus}$ (Leleu et al. 2022). Class-A lmUSPs can also have longer orbital periods. Examples for class-A planets that are not USPs are K2-3 b,c (Damasso et al. 2018; Kosiarek et al. 2019; Diamond-Lowe et al. 2022), and HD 219134 b (Motalebi et al. 2015; Vogt et al. 2015; Dorn et al. 2019; Ligi et al. 2019).

There are mainly two possibilities what class-A planet could be. One is that they contain low-density material like water ice, or Aluminium-rich minerals. Dorn et al. (2019) showed that Ca- and Al-rich minerals may be enhanced in lmUSPs that formed close to the star.

Another possibility is that class-A planets have hybrid atmospheres (Tian & Heng 2023). The outgassing hypothesis is plausible, because USPs are likely to have lava oceans (Barnes et al. 2010; Briot & Schneider 2010). Close-in rocky planets could also have exospheres like Mercury (Elkins-Tanton 2008; Mura et al. 2011).

There is indirect evidence that at least some class-A planets could have an atmosphere. Infrared observations of 55 Cnc e show that the hottest point is not at the substellar point, but east of it. This can best be explained by an atmosphere (Angelo & Hu 2017). Ridden-Harper et al. (2016) and Tsiaras et al. (2016) claimed to have detected the atmosphere directly, but this was not confirmed by Esteves et al. (2017) and Tabernero et al. (2020). *HST* observations of π Men c showed that it has a hybrid atmosphere (García Muñoz et al. 2021). In contrast to 55 Cnc e, phase curves of the lmUSP K2-141 b do not show any significant thermal hotspot offset. A rock vapour model and a 1D turbulent boundary layer model both fits well to the observations (Zieba et al. 2022).

At the present stage it is not known what the structure and composition of class-A planets is. We thus prefer to define the planets on the basis of their density, rather than composition.

Because class-C planets have a high density, they must have relatively large cores. However, the main issue for many UPSs is that the density measurements are not precise enough to conclude whether they are class-B, or class-C.

Possibly the best case for a class-C planet is the USP GJ367 b (Lam et al. 2021; Goffo et al. 2023). Although Brandner et al. (2022) obtained a smaller mass and larger radius for the planet than Lam et al. (2021) and Goffo et al. (2023), this planet still falls into class-C.

Other examples for class-C planets are K2-229 b, (Santerne et al. 2018), and HD80653 b (Frustagli et al. 2020). Although the masses of KOI 1843.03 and K2-137b have not been determined yet, the Roche limit implies mean densities of $\rho_{\rm p} > 7\,{\rm g\,cm^{-3}}$ for KOI 1843.03 (Rappaport et al. 2013), and $\rho_{\rm p} > 6.4\,{\rm g\,cm^{-3}}$ for K2-137b (Smith et al. 2018), respectively. KOI 1843.03 and K2-137b must therefore be class-C planets. A disputed case is K2-106 b.

Like class-A planets, class-C planets can also have orbital periods longer than 1 d. An example for a class-C planet that is not a USP is HD 137496 b (Azevedo Silva et al. 2022).

There is thus evidence that class-C planets exist but how did they form? An interesting case is the Kepler-107 system, because the inner planet is in class-B, and the outer in class-C. Because of this unusual architecture, Bonomo et al. (2019) argue that Kepler-107 c is the result of a giant impact that removed the outer layers of the planet.

Does this mean that all class-C planets are the result of impact stripping? This is not the case. Reinhardt et al. (2022) investigated how mantle stripping by giant impacts changes the composition of planets. Adibekyan et al. (2022) showed that the iron-mass fraction of planets is on average higher than that of the primordial values, and Scora et al. (2020) studied the composition of rocky exoplanets in the context of the composition of the stars. The result is that the composition of rocky planets spans a much wider range than that of stars. Super-Mercuries and super-Earths appear to be two distinct groups of planets. Mantle stripping alone thus cannot explain all class-C planets, formation and stripping both play a role.

Previous studies thus have shown that all three classes exist amongst USPs as well as for planets with longer periods. Studying USPs has the advantage that we can measure their masses and radii more precisely. USPs may have atmospheres but extended H/He atmospheres have not yet been found amongst lmUSPs.

Unfortunately, masses and radii of only a few USPs have been determined accurately enough to categorize them (Plotnykov & Valencia 2020). The most recent radius and mass distribution of USPs has been published by Uzsoy et al. (2021). However, not only accurate measurements are important, it is also important which theoretical mass–radius relation is used. For example, it makes a difference whether we use the relation from Wagner et al. (2011), Hakim et al. (2018), or Zeng et al. (2019). Thus, up to now there are only few planets that can be firmly categorized. Any additional object is important.

K2-106 b is a particularly interesting planet, because it orbits a relatively bright star; it is one the most massive rocky USPs known, and contradicting density measurements have been published (Guenther et al. 2017; Sinukoff et al. 2017; Dai et al. 2019; Singh et al. 2022; Rodríguez Martínez et al. 2023). It could thus either be of class-A, or B. K2-106 b was discovered by Adams et al. (2017) using K2-data. Previous mass, radius, and density values that were derived for K2-106 b are given in Table 1.

Another interesting property of K2-106 b is that it has a very high maximum geometric albedo of 0.9 ± 0.3, and a maximum dayside temperature of 3620^{+56}_{-53} K (Singh et al. 2022). A lava ocean of that temperature is expected to have a high albedo (Rouan et al. 2011). K2-106 c has the same mass as K2-106 b, but a lower density.

The mass and radius measurements can now be significantly improved. The radius of the star was originally determined using *Gaia* DR1, or by the analysis of stellar spectra. The improvement when using *Gaia* DR3 compared to DR1 is quite significant. The *Gaia* DR1 parallax was 3.96 ± 0.78 mas and the parallax from *Gaia*

Table 1. Radius, mass, and density of K2-106 b from the literature.

Rp [$R_{\oplus}$]	Mp [$M_{\oplus}$]	Density [g cm^{-3}]	Reference
$1.82^{+0.20}_{-0.14}$	9.0 ± 1.6	$8.57^{+4.64}_{-2.80}$	Sinukoff et al. (2017)
1.46 ± 0.14	–	–	Adams et al. (2017)
1.52 ± 0.16	$8.36^{+0.96}_{-0.94}$	$13.1^{+5.4}_{-3.6}$	Guenther et al. (2017)
2.31 ± 0.16	–	–	Livingston et al. (2018)
1.712 ± 0.068	$7.72^{+0.80}_{-0.79}$	8.5 ± 1.9	Dai et al. (2019)
1.6 ± 0.1	–	–	Adams et al. (2021)
$1.71^{+0.069}_{-0.057}$	8.53 ± 1.02	$9.4^{+1.6}_{-1.5}$	Rodríguez Martínez et al. (2023)
1.725 ± 0.039	$8.21^{+0.76}_{-0.74}$	$8.77^{+1.00}_{-0.94}$	Bonomo et al. (2023)

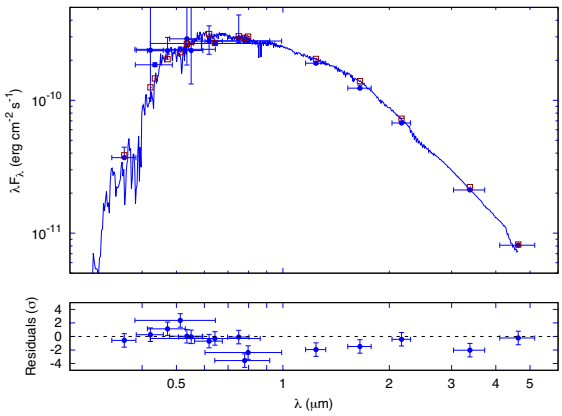

Figure 1. SED and the fit obtained with ARIADNE. The lower panel shows the residuals.

DR3 is 4.085 ± 0.018 mas (Gaia Collaboration 2021). Additional transits were observed by *TESS*, and we have obtained additional spectra with ESPRESSO. The ESPRESSO spectra have a higher resolution, a higher S/N, and a much higher RV accuracy. The higher resolution and the higher S/N allows to determine the mass and radius of the star to a higher accuracy. The new data allow to find out whether K2-106 b is in class-A, or in class-B.

2 OBSERVATIONS AND RESULTS

In the following sections we present new determinations of the fundamental parameters of the host star and compare them with previous estimates.

2.1 Mass, radius, and other stellar parameters derived from stellar magnitudes and *Gaia* DR3 parallax

The combination of *Gaia* parallax with broad-band photometry allows one to determine the radius of a star (see e.g. Stassun et al. 2018). The parallax of K2-106 is reported to be $\pi = 4.085 \pm 0.018$ μas in the *Gaia* Data Release 3 (*Gaia* DR3; Gaia Collaboration 2021).

Using the spectral energy distribution (SED)-fitting algorithm ARIADNE[1] (spectrAl eneRgy dIstribution bAyesian moDel averagiNg fittEr; Vines & Jenkins 2022), we obtain the parameters given in Table 4. With ARIADNE we derive $R_* = 1.039^{+0.025}_{-0.023}\,R_\odot$ and $M_* = 1.046^{+0.046}_{-0.053}$ using the MIST isochrones. ARIADNE uses the following magnitudes for K2-106: 2MASS J, H, K, Johnson V, B, Tycho B, V, *Gaia* G, Rp, Bp, SDSS g', r', i', WISE, W1, W2, and *TESS*. Since the SDSS z' magnitude is a clear outlier, we did not include it in the fit. ARIADNE uses a number of different stellar models (Phoenix V2 (Brott & Hauschildt 2005), BT-Models (https://osubdd.ens-lyon.fr/phoenix/), and the Kurucz models (Castelli & Kurucz 1993; Kurucz 1993). Shown in Fig. 1 are the Kurucz models together with the photometric measurements. The SED fit shows that is a main-sequence star. The values obtained with are listed in Table 2.

We also determine the mass and radius, as well as other stellar parameters using the isochrones code (Morton 2015) using with the MESA isochrones (Choi et al. 2016; Dotter 2016). This method utilizes a multimodal nested sampler `multinest` (Feroz & Hobson 2008; Feroz, Hobson & Bridges 2009; Feroz et al. 2019) to sample 1000 live points with following input and errors of the values: $T_{\rm eff} = 5493$ K [5433 to 5553 K], [Fe/H] $= -0.11$ [-0.11 to $+0.11$], parallax: 4.085 mas [4.035 to 4.135 mas], and using the brightness values listed in Table 3. Instead of B and V we used the *Gaia* values because they are more precise. We also tried out using the B and V instead of the *Gaia* values but did not find a significant difference. This global fit takes the respective uncertainties into account, and the value derived can exceed the uncertainty of a specific input value. Fig. 2 shows the mass and radius values of the host star obtained in this work with the literature. With ISOCHRONES we derive $R_* = 0.990 \pm 0.012\,R_\odot$ and $M_* = 0.913 \pm 0.024$.

The radius of the star can also be obtained by combining the *Gaia* parallax and the 2MASS photometry (Skrutskie et al. 2006) as described in Guenther et al. (2021). Using this method, we obtain $R_* = 0.989 \pm 0.022\,R_\odot$. This method has the advantage that it is less affected by interstellar absorption, because it uses only infrared colours. However, the extinction should not play a significant role given that the star has a Galactic longitude $l = 123.2°$, Galactic latitude $b = -51.1°$, and a distance of 244.8 ± 1.1 pc.

[1] Available at https://github.com/jvines/astroARIADNE.

Table 2. Properties of the host star derived from *Gaia* data and using from *Gaia* using ARIADNE and from isochrones.

Parameter	*Gaia*	ARIADNE	ISOCHRONES
RA (J2000.0)[a]	00:52:19.1		
DE (J2000.0)[a]	+ 10:47:40.91		
pm RA [mas yr^{-1}][a]	61.01 ± 0.02		
pm RA [mas yr^{-1}][a]	2.06 ± 0.01		
RV [km s^{-1}][a]	-14.79 ± 0.56		
Parallax [mas][a]	4.09 ± 0.02		
Distance [pc]	244.8 ± 1.1		
R_*[$R_\odot$]		$1.039^{+0.025}_{-0.023}$	0.990 ± 0.012
M_* [$M_\odot$]		$1.046^{+0.046}_{-0.053}$[b]	0.913 ± 0.024
$T_{\rm eff}$ [K]		5493^{+57}_{-61}	5578 ± 46
Luminosity [$L_\odot$]		$0.885^{+0.057}_{-0.054}$	
log(g)		$4.421^{+0.076}_{-0.068}$ $4.26^{+0.08}_{-0.08}$	4.408 ± 0.017
[Fe/H]		$-0.11^{+0.11}_{-0.11}$	-0.005 ± 0.059
Extinction Av		$0.098^{+0.040}_{-0.044}$	0.219 ± 0.038

Note. [a]*Gaia* DR3 2582617711154563968. [b]Mass derived by interpolating MIST isochrones.

Table 3. Brightness of the star.

Band	Mag
V	12.58 ± 0.26
B	12.10 ± 0.21
Gaia G	11.9438 ± 0.0028
Gaia BP	12.3315 ± 0.0028
Gaia RP	11.3935 ± 0.0038
Tycho B_T'	12.67 ± 0.26
Tycho V_T'	12.16 ± 0.21
SDSS g'	12.629 ± 0.010
SDSS r'	12.0262 ± 0.0095
SDSS i'	11.812 ± 0.0100
TESS	11.457 ± 0.078
J	10.77 ± 0.023
H	10.454 ± 0.026
Ks	10.344 ± 0.021
WISE 1	10.299 ± 0.023
WISE 2	10.355 ± 0.021
WISE 3	10.380 ± 0.091

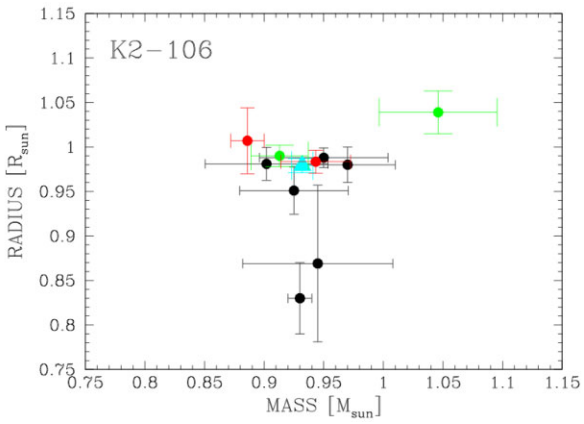

Figure 2. Mass and radius of the star. Values from the literature (black), average value from the literature (blue triangle), the new value derived from ESPRESSO spectra (red), and the new value from *Gaia* EDR3 using ARIADNE (MIST isochrones) and isochrones (green).

We also determined the stellar mass and radius using the online version of EXOFASTv1 (Eastman, Gaudi & Agol 2013).[2] The mass of the star as obtained with $\mathcal{X}^2$ fitting algorithm is $M_* = 0.96 \pm 0.01\,M\odot$ and with the MCMC algorithm we obtained $M_* = 0.96^{+0.05}_{-0.04}\,M\odot$. For the stellar radius, we derive $R_* = 0.92 \pm 0.17\,R_\odot$ with $\mathcal{X}^2$ fitting algorithm, and $R_* = 1.00^{+0.04}_{-0.04}$ with the MCMC. As shown in Table 4, these values are also in agreement with other values for mass and radius, derived in this work.

2.2 Mass, radius, and other stellar parameters derived from ESPRESSO spectra

We acquired 23 spectra of K2-106 using the ESPRESSO spectrograph (Pepe et al. 2014, 2021) at the VLT UT3 (Melipal) as part of program 0103.C-0289(A). The spectra were obtained from 2019 August 8 to 2019 November 16. We used the high-resolution mode which gives a resolving power of $\lambda/\Delta\lambda \sim 140\,000$. The spectra cover the wavelength range from 3782 to 7887 Å. All calibration frames were taken using the standard procedures of this instrument. The spectra were reduced and extracted using the dedicated ESPRESSO pipeline.

We derived new values for $T_{\rm eff}$, log(g), and [Fe/H] using the six ESPRESSO spectra with the highest S/N ratio using the same method as described in Smith et al. (2019), Fridlund et al. (2020), Georgieva et al. (2021), Persson et al. (2022), Serrano et al. (2022), Georgieva et al. (2023), Lam et al. (2023), Osborn et al. (2023), Osborne et al. (2023), and Deeg et al. (2023). We fixed the micro- and macro-turbulence to $v_{\rm mic} = 0.9 \pm 0.1$ and $v_{\rm mac} = 1.70 \pm 0.35\,{\rm km\,s^{-1}}$, using the relations given by Doyle et al. (2014) and Bruntt et al. (2010), respectively. Fitting the H_α profile using Kurucz ATLAS12 models and spectra models (Kurucz 2013), we find $T_{\rm eff} = 5344 \pm 60$ K. This corresponds to a spectral type G9 V, according to the mean dwarf stellar colour and effective temperature sequence[3] from Pecaut, Mamajek & Bubar (2012).

The projected rotation velocity of the star is $v \sin i_\star = 2.7 \pm 0.4\,{\rm km\,s^{-1}}$, which gives a statistical age of $1.3^{+0.6}_{-0.3}$ Gyr (Maldonado et al. 2022). The v sin i has been determined using unblended Fe I lines. The activity index $\log(R'_{\rm HK})$ was already published in Guenther et al. (2017). On average it is $\log(R'_{\rm HK}) = -5.04 \pm 0.19$, which gives a statistical age of $7.4^{+3.0}_{-3.4}$ Gyr (Mamajek & Hillenbrand 2008). Based on CaIIHK-index K2-106 is an old, inactive star.

At first glance it appears the that relatively rapid rotation of the star contradicts the low $\log(R'_{\rm HK})$ index and the old age derived. However, the stellar spin-down can be affected by close-in planets (Benbakoura et al. 2019; Ilic, Poppenhaeger & Hosseini 2022; Guo 2023). A star hosting a close-in planet thus may rotate faster than a star without close-in planets.

Many planet host stars also have an abnormally low level Ca II H&K emission which is interpreted as a signature of atmospheric mass-loss from planets rather than a low activity level, or an old age of the host star (Haswell et al. 2012; Staab et al. 2020; Barnes et al. 2023). Given that both the rotation velocity and the Ca II H&K flux can be affected by a close-in planet, it is not surprising that we obtain contradicting results for the ages from these parameters.

Although the radius determination using *Gaia* parallax is expected to be more accurate, we also determined the log(g) using Ca I, Mg I, and Na I as an independent test. Determining the radius of a star from log(g) is less accurate then either using the stellar density derived from the light-curve fit, or the radius determined by combining the distance of the star combined with the SED. However, comparing the stellar density obtained from the spectral analysis with that obtained from the light-curve fitting of the star is a good test of the spectral analysis (Guenther et al. 2012). The results of these tests are discussed in Section 2.3. Using Ca I we derive $\log(g) = 4.20 \pm 0.06$, using Mg I $\log(g) = 4.26 \pm 0.08$, and using Na I $\log(g) = 4.2 \pm 0.04$. Given the temperature of this star, the value derived from the Mg I is the most accurate. We obtain the element abundances of iron $[{\rm Fe/H}] = -0.03 \pm 0.05$ (dex), calcium $[{\rm Ca/H}] = -0.03 \pm 0.05$ (dex), sodium $[{\rm Na/H}] = 0.00 \pm 0.05$ (dex), and magnesium $[{\rm Mg/H}] = -0.03 \pm 0.05$ (dex).

Using $T_{\rm eff}$, log(g), and [Fe/H] derived spectroscopically, the Bayesian estimation of stellar parameters, and the MESA isochrones (da Silva et al. 2006; Rodrigues et al. 2014, 2017) we obtain $R_* = 1.007^{+0.050}_{-0.024}\,R_\odot$ and $M_* = 0.886^{+0.014}_{-0.014}\,M_\odot$. The mass and radius of the star derived spectroscopically and using SED-fitting are independent from each other, since we used $T_{\rm eff}$ and [Fe/H] only as priors for the SED fitting.

We also made a second analysis of the ESPRESSO spectra. Adding up all ESPRESSO spectra, weighted by their signal-to-noise ratio, we obtain a spectrum with a S/N of 228. We then obtained the equivalent width of the Fe I and Fe II lines from the ispec framework (Blanco-Cuaresma et al. 2014; Blanco-Cuaresma 2019). The equivalent widths are then fitted to ATLAS (LTE) model atmospheres (Kurucz 2005). The chemical abundances are determined using the stellar atmosphere modeling code SYNTHE which is using the radiative transfer code WIDTH (Sbordone et al. 2004).

From this analysis we obtain $T_{\rm eff} = 5488 \pm 60$ K, $\log(g) = 4.28 \pm 0.2$, and $[{\rm FeH}] = 0.04 \pm 0.08$. Converting again these values into the mass, radius, and age of the star gives $M_* = 0.943 \pm 0.029\,M\odot$, $R_* = 0.983 \pm 0.013\,R\odot$, and 7.3 ± 2.0 Gyr, respectively. Using these parameters gives a distance of $d = 244.6 \pm 2.9$ pc in perfect agreement with the distance determined by *Gaia*. Both mass and radius values derived in this section are shown as red points in Fig. 2.

2.3 Comparing the new mass and radius determination of the host star with previously determinations

As mentioned above, the mass, radius, and temperature of the host star has already been determined previously (Adams et al. 2017,

[2] https://exoplanetarchive.ipac.caltech.edu/cgi-bin/ExoFAST/nph-exofast

[3] Available at https://www.pas.rochester.edu/~emamajek/EEM_dwarf_UBVIJHK_colors_Teff.txt.

Table 4. Radius, mass, temperature, and log(g) of the host star from the literature and derived in this work.

R_* [R⊙]	M_* [M⊙]	T_{eff} [K]	log(g)	[Fe/H] dex	Reference
0.83 ± 0.04	0.93 ± 0.01	5590 ± 51	4.56 ± 0.09	0.025 ± 0.02	Adams et al. (2017)
0.869 ± 0.088	0.945 ± 0.063	5470 ± 30	4.53 ± 0.08	-0.025 ± 0.05	Guenther et al. (2017)
0.98 ± 0.02	0.97 ± 0.04	5617 ± 86	4.45 ± 0.03	0.13 ± 0.06	Livingston et al. (2018)
$0.981^{+0.019}_{-0.018}$	$0.902^{+0.057}_{-0.046}$	5496 ± 46	4.42 ± 0.05	0.06 ± 0.03	Dai et al. (2019)
0.95 ± 0.05	–	5613 ± 39	4.60 ± 0.07	0.01 ± 0.01	Adams et al. (2021)
$0.951^{+0.027}_{-0.026}$	$0.925^{+0.049}_{-0.042}$	5598^{+80}_{-78}	$4.449^{+0.031}_{-0.029}$	$0.096^{+0.060}_{-0.058}$	Singh et al. (2022)
0.988 ± 0.011	$0.950^{+0.060}_{-0.048}$	5532 ± 62	–	0.11 ± 0.05	Bonomo et al. (2023)
0.979 ± 0.008	0.932 ± 0.009	5535 ± 18	4.46 ± 0.02	0.022 ± 0.008	average of Literature values
$1.007^{+0.050}_{-0.024}$	$0.886^{+0.014}_{-0.014}$	5344 ± 60	$4.26^{+0.08}_{-0.08}$	-0.03 ± 0.05	ESPRESSO[a]
0.983 ± 0.013	0.943 ± 0.029	5488 ± 60	4.28 ± 0.20	0.04 ± 0.08	ESPRESSO[b]
$1.039^{+0.025}_{-0.023}$	$1.05^{+0.19}_{-0.17}$	5493^{+57}_{-61}	$4.421^{+0.076}_{-0.068}$	-0.11 ± 0.11	SED + *Gaia* DR3[c]
$1.039^{+0.025}_{-0.023}$	$1.046^{+0.046}_{-0.053}$	5493^{+57}_{-61}	$4.421^{+0.076}_{-0.068}$	-0.11 ± 0.11	SED + *Gaia* DR3[d]
0.989 ± 0.022					2MASS + *Gaia* DR3[e]
0.990 ± 0.012	0.913 ± 0.024	5578 ± 46	4.408 ± 0.017	-0.05 ± 0.06	ISOCHRONES
0.993 ± 0.008	0.907 ± 0.011	5491 ± 28	4.402 ± 0.016	-0.02 ± 0.03	average this work

Note. [a]Mass and radius calculated from modelling the ESPRESSO spectra using the Kurucz ATLAS12 models and the MESA isochrones. See Section 2.2 for details. [b]Mass and radius calculated using ESPRESSO spectra, the Fe I, Fe II lines, and the WIDTH radiative transfer code. See Section 2.2 for details. [c]Mass calculated directly from the star's log g and R_*. [d]Mass derived by interpolating MIST isochrones. [e]Method described in Guenther et al. (2021).

2021; Guenther et al. 2017; Sinukoff et al. 2017; Dai et al. 2019; Singh et al. 2022; Rodríguez Martínez et al. 2023). How do the new values compare to the previous determinations? The mass, radius, T_{eff}, and, [Fe/H] from the literature and derived in this work are given Table 4.

In Fig. 2 we compare the mass and radius measurements obtained for the host star from the literature (black points individual measurements, blue triangle average), with the spectroscopic determination (red points), and with the values obtained using ARIADNE and ISOCHRONES (green points).

Since ARIADNE and ISOCHRONES take advantage of the accurate distance determination obtained in *Gaia* DR3, these values are the preferred ones. Some of the previous determinations are based on *Gaia* DR1, or *Gaia* DR2, and thus have larger errors compared *Gaia* DR3.

There is another possibility to verify the mass and radius derived for the star. As explained in Section 2.6, the density of the star can also be derived from light-curve fitting. Comparing the stellar density derived from the light-curve and stellar modelling thus is an excellent test.

2.4 The radii of the planets in respect to the radius of the host star

2.4.1 Analysis of the K2 and TESS *light curves*

As the name already indicates, K2-106 was originally found in the K2 survey. 136 transits were obtained during the K2-mission. Up to now, only 12 transits have been observed with the *TESS* satellite. The cadence time of K2 data is 30 min. We supersampled the transit model by a factor of 10 to account for the K2 long-cadence data as described in (Kipping 2010; Barragán, Gandolfi & Antoniciello 2019a). The quality of the *TESS* light curves is much lower than those obtained in the K2 mission. We therefore use only the K2 data for the radius determination, and the K2 together with the *TESS* for the ephemeris. There are several ways how to extract the light curves, how to remove the instrumental effects, and how to remove stellar activity. The star is, however, quite inactive. We tried out the light curves provided by Vanderburg & Johnson (2014), and those obtained with the K2SC algorithm (Aigrain, Parviainen & Pope 2016).[4]

Fig. 5 shows the values obtained for the two light curves with and without using the stellar density derived as an informative prior (See Section 2.6 for details). Both light curves gave consistent results, but the errors are smaller for the K2SC data.

As described in detail in Section 2.6, we model the light curves and the RV curve together. We included a photometric jitter term in the fit to account for instrumental noise that is not included in the nominal error bars. The photometric jitter term for K2 is $\sigma_{K2} = 0.0000882 \pm 0.0000018$. Figs 3 and 4 show the fit to the phase-folded light curves using the combined model. Outliers were removed using 3σ clipping criterion.

The RV measurements are discussed in Section 2.5. The off-sets between different instruments and their jitter terms are given in Table 5 and Table 6.

2.4.2 Comparing the ratio of the radius of the planets to the host star with previous determinations

Fig. 5 shows the previous determinations of the ratio of the radii of the planets to the radius of the host star. The black points are values taken from the literature (Adams et al. 2017; Guenther et al. 2017; Sinukoff et al. 2017; Dai et al. 2019; Singh et al. 2022; Rodríguez Martínez et al. 2023). Since Dai et al. (2019) and Singh et al. (2022) did not publish the values for K2-106 c we simply used the average Rp/R_{star} values for K2-106 c from the literature to show the values for K2-106 b in this figure. The ratio of the radius of K2-106 b to the host star is within the errors the same. Using the variance as the

[4]https://archive.stsci.edu/prepds/k2sc/

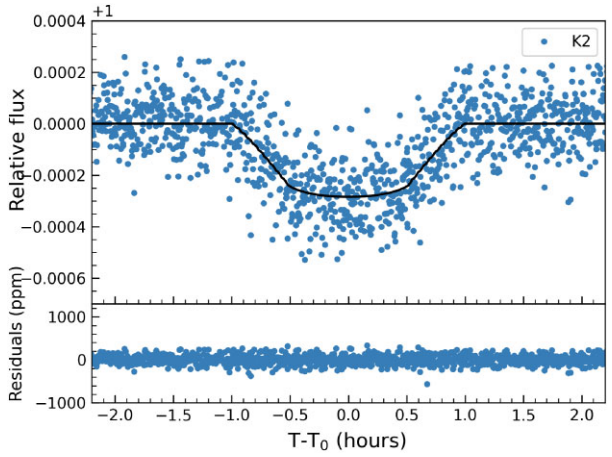

Figure 3. Phase-folded light curve obtained with K2 of K2-106 b, after removing a few outlier using a 3σ clipping.

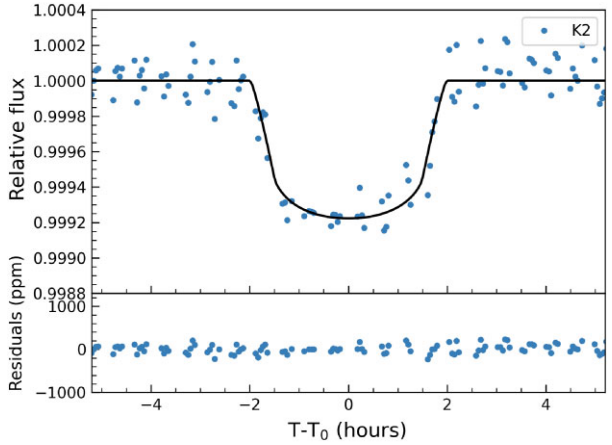

Figure 4. Phase-folded light curve obtained with K2 of K2-106 c after removing a few outlier using a 3σ clipping.

error it is $R_{K2-106b}/R_{star} = 0.0160 \pm 0.0006$, and $R_{K2-106c}/R_{star} = 0.0270 \pm 0.0009$, respectively. We also show the radius ratios derived in Section 2.4.1 as red points. The new determinations of the ratios of the radii of the planets to the host stars are in line with the previous determinations.

2.5 RV measurements obtained with ESPRESSO combined with previous measurements

We obtained 23 new RV measurements of K2-106 with the ESPRESSO spectrograph that were reduced and extracted using the dedicated ESPRESSO pipeline (Pepe et al. 2021). The RVs were determined using a cross-correlation method with a numerical mask that corresponds to a G8 star. The RVs were obtained in the usual manner by fitting a Gaussian function to the average cross-correlation function (Baranne et al. 1996; Pepe et al. 2021). The data reduction pipelines of this instrument also provides the absolute RV. The median error for the ESPRESSO data is 1.7 ms^{-1}. For comparison, the 32 HARPS spectra that we used previously had a median error of 3.2 ms^{-1}, the 13 PSF spectra 3.0 ms^{-1}, the three HDS spectra 5.0 m s^{-1}, and the six FIES spectra 4.8 ms^{-1} (Guenther et al. 2017).

Because our main interest is the mass determination of the inner planet K2-106 b, we decided to take several spectra per night when possible. The RV-values obtained with ESPRESSO are listed in Table 5.

In order to combine the RVs obtained previously with the ESPRESSO data, we determined instrumental off-sets between the instruments and the jitter-terms. The off-sets and jitter-terms are listed in Table 6. The accuracy of the RVs obtained with ESPRESSO is higher than that of the other instruments but the high jitter term indicates that the star was a bit more active during ESPRESSO observations. Figs 6 and 7 show the phase-folded RV curves of K2-106b and K2-106c, respectively.

2.6 Radii and masses of the two planets

The mass and radius of the host star are key factors for the determination of the masses and radii of planets. As explained in Sections 2.3, 2.2, and 2.1, we obtained six different sets of stellar parameters. However, if we do not count 2MASS-*Gaia* DR3 method, because it gives only the radius of the star, and the value derived directly from the log(g) and R_*, we have obtained four new values for the mass and radius of the star.

We determined the masses and radii of the planets using the PYANETI-code (Barragán et al. 2019a; Barragán et al. 2022a). PYANETI performs a multiplanet radial velocity and transit data fitting. The code uses a Bayesian approach combined with a Markov chain Monte Carlo sampling to estimate the parameters of planetary systems. We added a photometric and an RV jitter term to account for instrumental noise not included in the nominal uncertainties. We used the standard set up previously used in other articles (Barragán et al. 2019b, 2022b, 2023; Georgieva et al. 2021; Persson et al. 2022; Serrano et al. 2022). A good sampling is assured using a number of chains which is at least as twice as the amount of parameters. We sampled the parameter space using 500 Markov chains. We created the posterior distributions using the last 5000 iterations of the converged chains with a thin factor of 10. We used the convergence test developed by Gelman & Rubin (1992), as described in Barragán et al. (2019b). This approach leads to a distribution of 250 000 points for each model parameter per distribution. The best estimates and their 1σ uncertainties were taken as the median and the 68 per cent limits of the credible interval of the posterior distributions.[5]

We obtained the density of the star from the light curve without using stellar density as informative prior and also using the stellar density as an uninformative prior. We did not find any significant difference between the two. Using the stellar density obtained with ISOCHRONES as a informative prior we obtain from the light-curve modelling of the inner planet a stellar density of $\rho_{star} = 1.349^{+0.089}_{-0.089}$ g cm^{-3}. We did the same analysis using the stellar density from ARIADNE as informative prior. In this case we obtain $\rho_{star} = 1.348^{+0.116}_{-0.106}$ g cm^{-3}. The difference is insignificant but the errors are larger if we use the ARIADNE values.

We can also compare the stellar density derived from the light curve with the stellar density derived from the four methods described in Sections 2.1 and 2.2. This is possible, because the density of the star can be determined from the light curve without knowing the mass and radius of the host star (Sandford & Kipping 2017). We find that

[5]In Barragán et al. (2019b), they defined convergence as when chains have a scaled potential factor $\mathrm{R} = \sqrt{[W(n-1)/n + B/n]/W} < 1.02$ for all the parameters (Gelman et al. 2004), where B is the 'between-chain' variance, W is the 'within-chain' variance, and n is the length of each chain.

Table 5. Radial velocities obtained with ESPRESSO.

BJD_{TDB} −2450000	RV [km s^{-1}]	FWHM [km s^{-1}]	BIS [km s^{-1}]	S/N
8703.75031525	−15.8276 ± 0.0034	7.46347 ± 0.0067	−0.0931 ± 0.0067	29.4
8704.91475462	−15.8232 ± 0.0018	7.48160 ± 0.0038	−0.0952 ± 0.0037	43.5
8705.75671620	−15.8180 ± 0.0045	7.49173 ± 0.0089	−0.0965 ± 0.0089	24.7
8707.81075258	−15.8176 ± 0.0022	7.48481 ± 0.0044	−0.0923 ± 0.0044	38.9
8707.90836233	−15.8198 ± 0.0016	7.48639 ± 0.0032	−0.0876 ± 0.0032	47.6
8708.74798097	−15.8278 ± 0.0017	7.48843 ± 0.0035	−0.0877 ± 0.0035	45.4
8709.77704796	−15.8243 ± 0.0011	7.48605 ± 0.0023	−0.0883 ± 0.0023	61.2
8709.79036694	−15.8258 ± 0.0013	7.48668 ± 0.0025	−0.0921 ± 0.0025	56.6
8717.72563374	−15.8264 ± 0.0021	7.47178 ± 0.0042	−0.0896 ± 0.0042	40.1
8717.82099476	−15.8283 ± 0.0013	7.48843 ± 0.0026	−0.0926 ± 0.0026	54.5
8718.74229989	−15.8179 ± 0.0017	7.48184 ± 0.0033	−0.0882 ± 0.0033	46.8
8718.87715170	−15.8248 ± 0.0015	7.48387 ± 0.0030	−0.0945 ± 0.0030	50.1
8719.86954645	−15.8157 ± 0.0011	7.48672 ± 0.0021	−0.0907 ± 0.0021	62.3
8721.69988499	−15.8153 ± 0.0024	7.50070 ± 0.0048	−0.0895 ± 0.0048	36.7
8724.71755081	−15.8268 ± 0.0016	7.48293 ± 0.0033	−0.0960 ± 0.0033	47.2
8777.68002329	−15.8223 ± 0.0013	7.48530 ± 0.0026	−0.0950 ± 0.0026	50.5
8782.52691959	−15.8355 ± 0.0020	7.47913 ± 0.0040	−0.0942 ± 0.0040	36.8
8782.61367352	−15.8262 ± 0.0014	7.49631 ± 0.0028	−0.0957 ± 0.0028	46.9
8784.63761295	−15.8291 ± 0.0018	7.48978 ± 0.0036	−0.0915 ± 0.0036	54.6
8788.76247468	−15.8275 ± 0.0024	7.50070 ± 0.0048	−0.0898 ± 0.0048	32.4

Table 6. Off-sets and jitter-terms.

Instrument	off-set [m s^{-1}]	jitter [m s^{-1}]
HIRES	$-22.22^{+0.88}_{-0.88}$	$4.79^{+0.74}_{-0.60}$
PSF	$0.63^{+1.77}_{-1.85}$	$5.36^{+2.07}_{-1.68}$
HDS	$24.28^{+4.84}_{-4.57}$	$3.94^{+9.48}_{-3.21}$
FIES	$98.92^{+2.32}_{-2.36}$	$1.24^{+2.48}_{-0.95}$
HARPS-N	$-15736.08^{+1.09}_{-1.10}$	$1.37^{+1.48}_{-1.01}$
HARPS:	$-15732.63^{+0.83}_{-0.85}$	$1.31^{+1.21}_{-0.95}$
ESPRESSO:	$-15823.74^{+0.73}_{-0.73}$	$2.74^{+0.70}_{-0.56}$

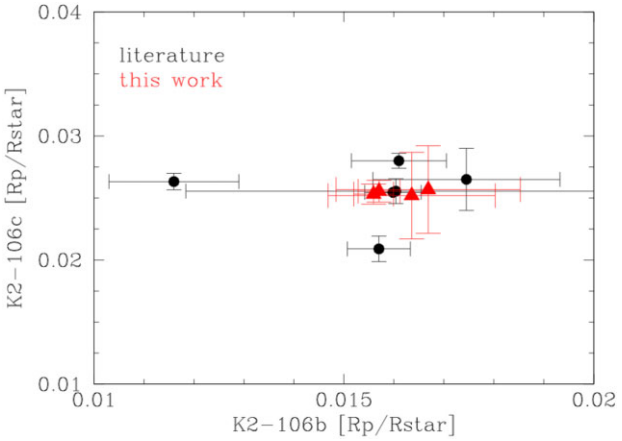

Figure 5. Ratio of the radius of the planets K2-106 b and K2-106 c to the radius of the host star. Values from the literature (black), and the values derived in this work (red triangle).

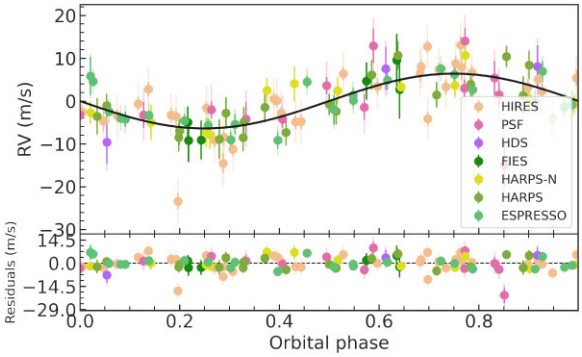

Figure 6. Phase-folded RV curve of K2-106 b.

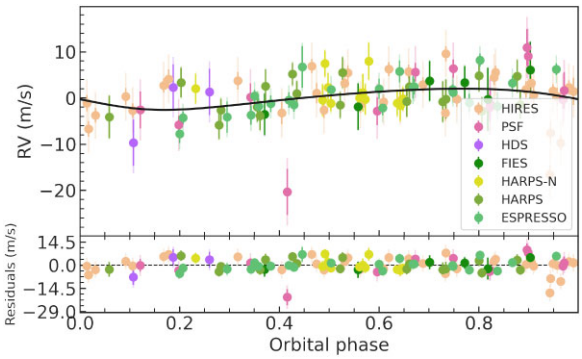

Figure 7. Phase-folded RV curve of K2-106 c.

the difference is smallest for the stellar parameters obtained using ISOCHRONES. The stellar density derived from the mass and radius using ISOCHRONES is $\rho_{star} = 1.327^{+0.060}_{-0.058}$ g cm^{-3}. With ARIADNE we obtain $\rho_{star} = 1.315^{+0.116}_{-0.106}$ g cm^{-3}. In Section 2.5 we also derived the mass and radius of the star using the stellar parameters derived from the ESPRESSO spectra. Using these values we obtain densities of $1.22^{+0.17}_{-0.09}$ and 1.40 ± 0.07 g cm^{-3} for the star, respectively.

The difference between the density derived from the four sets of stellar parameters, and from the light-curve fitting are thus small,

Table 7. Parameters K2-106 b and K2-106 c.

Parameter	K2-106 b	K2-106 c
T_0	$2457394.00907^{+0.00067}_{-0.00069}$	$2457405.7320^{+0.0016}_{-0.0016}$
P [d]	0.5713127 ± 0.0000055	$13.33989^{+0.00068}_{-0.00070}$
e	0.0	$0.17^{+0.11}_{-0.11}$
b	$0.24^{+0.11}_{-0.14}$	$0.53^{+0.13}_{-0.20}$
a/R_*	$2.855^{+0.065}_{-0.065}$	$23.32^{+0.50}_{-0.53}$
Rp/R_*, K2	$0.01553^{+0.00029}_{-0.00028}$	$0.02659^{+0.00080}_{-0.00073}$
i [deg]	$85.2^{+2.9}_{-2.4}$	$88.62^{+0.40}_{-0.17}$
a/R_*, K2	$2.855^{+0.061}_{-0.065}$	$23.32^{+0.50}_{-0.52}$
a [AU]	$0.01314^{+0.00032}_{-0.00034}$	$0.1073^{+0.0026}_{-0.0027}$
depth, K2 [ppm]	$241.0^{+9.0}_{-8.7}$	693^{+47}_{-36}
T_{tot}[h]	$1.540^{+0.033}_{-0.031}$	$3.661^{+0.078}_{-0.073}$
T_{full}[h]	$1.487^{+0.034}_{-0.033}$	$3.389^{+0.075}_{-0.085}$
$T_{in/eg}$[h]	$0.026^{+0.002}_{-0.001}$	$0.130^{+0.041}_{-0.028}$
K [m s^{-1}]	$6.36^{+0.57}_{-0.57}$	$2.14^{+0.74}_{-0.69}$
M_p [$M_\oplus$]	$7.80^{+0.71}_{-0.70}$	$7.32^{+2.49}_{-2.38}$
R_p, K2 [$R_\oplus$]	1.676 ± 0.037	$2.84^{+0.10}_{-0.08}$
ρ_p [g cm^{-3}]	9.09 ± 0.98	$1.72^{+0.66}_{-0.58}$
T^a_{eq} [K]	2299^{+36}_{-35}	804^{+13}_{-12}
λ^b	$15.3^{+1.5}_{-1.4}$	24^{+8}_{-8}
Insolation [$F_\oplus$]	4656^{+300}_{-274}	70^{+5}_{-4}

Notes. [a]$T_{eq} = T_{eff}\sqrt{\frac{R_*}{2a}}(1 - A_B)^{1/4}$, using an albedo $A_B = 0$.
[b]λ: Jeans escape parameter (Fossati et al. 2017).

especially for the stellar model derived from ISOCHRONES. The mass and radius derived from ISOCHRONES also match the average mass and radius values of the star from the literature best. Because the errors for the stellar model from ISOCHRONES are also smaller, we adopt these values. However, we will still discuss in Section 3 if it makes a difference if we use one of the other sets of stellar parameters.

The difference between stellar density from ISOCHRONES as an informative prior or as an uninformative prior are insignificant. If we use stellar density from ISOCHRONES as an informative prior or as an uninformative prior, we find for the inner planet: $Rp = 1.780^{+0.065}_{-0.061}\,R_\oplus$ versus $Rp = 1.767^{+0.062}_{-0.060}\,R_\oplus$ and $Mp = 8.61^{+0.84}_{-0.83}\,M_\oplus$ versus $Mp = 8.58^{+0.83}_{-0.80}\,M_\oplus$.

The results obtained for the two planets are listed in Table 7. The phase-folded light curves are shown in Figs 3 and 4. The RV curves are displayed in Figs 6 and 7. The posterior distributions of the parameters are shown in Figs A1 and A2.

3 DISCUSSION

The K2-106 system is one of the best systems for measuring the densities of low-mass planets, but what precision has been achieved?

The first error source is the radius and the mass of the host star. Some of the previous studies of this system have used older versions of the *Gaia* measurements. The *Gaia* DR3 measurements of the radius significantly improves the accuracy. We have determined the radius and the mass of the star using four different methods. The values from the literature and our new values are given in Table 4.

The density of the inner planet derived with ARIADNE is $8.25^{+1.15}_{-1.02}$ g cm^{-3}. With ISOCHRONES we obtain $9.09^{+0.98}_{-0.98}$ g cm^{-3}. Within the errors, the two values are the same. Taking the variance of the two values, the precision with which the density of the inner planet could be determined is 6.9 per cent. The density of K2-106 b has now been determined to a higher precision than for most other lmUSPs.

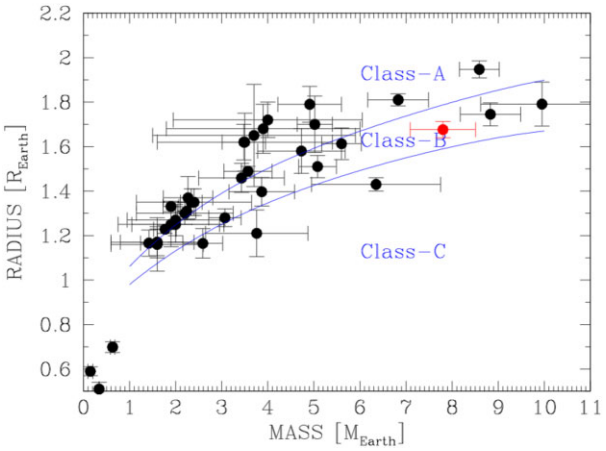

Figure 8. Mass–radius diagram for USPs. The red point is K2-106 b. The dark blue lines are the lower and upper limits for planets and Earth-like core radius fraction calculated by Hakim et al. (2018). The upper line represents a core which is composed of 80 per cent iron and 20 per cent other elements, and a mantle that is made of $MgSiO_3$. The lower curve is a pure Fe core with a $FeSiO_3$ mantle.

If we want to asses the nature of a planet we also have to take the errors of the theoretical models into account. Hakim et al. (2018) argue that it is not known what the exact composition of the core and mantle of an exoplanet is. They calculate the mass–radius diagram for planets with a Mercury-like, Earth-like, and Moon-like core-to-mantle fraction using four different mantle and six different core compositions. A planet with the highest density has pure Fe core and a Fe_2SiO_3 mantle. A rocky planet with the lowest density has a core that contains 80 per cent iron, and 20 per cent Aluminium and other light elements, and a $MgSiO_3$ mantle. In this model, planets with an Earth-like core-to-mantle ratio thus can have different densities, depending on the exact composition of the core and the mantle. We define a class-B planet as a planet that has the same core-to-mantle ratio as the Earth allowing for different compositions of the core and the mantle.

Fig. 8 shows the mass–radius measurements for known USPs including K2-106 b. The lines indicate the maximum and minimum radius for planets with the core-to-mantle ratios as the Earth. Fig. 9 shows the classical mass–radius diagram for USPs using the models published by Zeng et al. (2019). Many USPs fall into the regime of Class-B planets, but there are also many that are in Class-A.

K2-106 b is in Class-B, but this does not mean that K2-106 b must be Earth-like. Even if it would have a similar composition as the Earth, a USP is always unlike the Earth. For example, USPs have lava oceans because of the radiative heating by the host star (Barnes et al. 2010; Briot & Schneider 2010). Furthermore, USPs are not only radiatively heated but also tidally, magnetically, by flares, and by Coronal-Mass-Ejection (CME) from the host star (Kislyakova et al. 2017; Bolmont et al. 2020; Lanza 2021; Grayver et al. 2022). It is thus plausible that many lmUSPs have lava oceans and thus outgassed, or hybrid atmospheres. Such an atmosphere would then contain heavier, non-volatile elements. For example, Bower et al. (2022) showed that the atmospheres of planets with lava oceans should be carbon-rich. This means that although K2-106 b is a class Class-B planet, it does not have to have the same structure, and composition as the Earth. For example, K2-106 b could have a core that is larger than that of the Earth, and an atmosphere. At the present

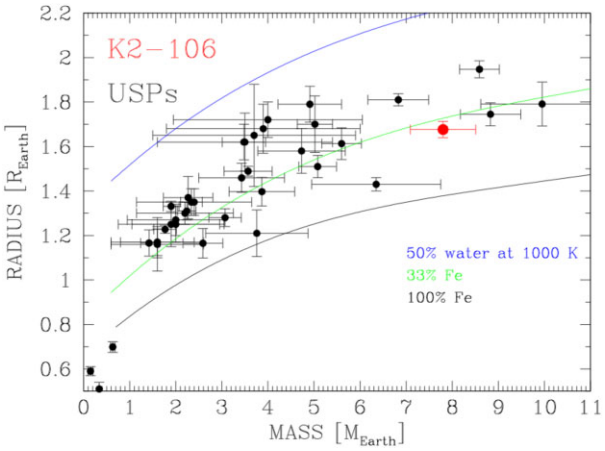

Figure 9. Classical mass–radius diagram for USPs. The red point is K2-106 b; the other points are the other USPs listed in Table 8. The mass–radius compositions for 100 per cent iron (black line), 33 per cent iron (green line), and 50 per cent water at 1000 K (blue line) are taken from Zeng et al. (2019).

stage, we do not even know whether K2-106 b is simply a bare rock, or a planet with a lava-ocean and an atmosphere.

Thus, additional observations are needed to find out what kind of a planet it is. First of all, we need to find out whether it has a lava ocean and an atmosphere or not. Zilinskas et al. (2022) have studied the observability of evaporating lava worlds, and Ito et al. (2015) have calculated the spectrum of an atmosphere composed of gas-species from a magma ocean. Phase curves of K2-106 b obtained with the *JWST* would allow to find out if there is a lava ocean and an atmosphere. Transit observations obtained with the *JWST*, or with CRIRES$^+$, would also allow us to find out what the composition of the atmosphere is, if the planet has one.

However, using a three-layer interior structure mode Suissa, Chen & Kipping (2018) have shown that planets with very different compositions can have the same bulk density. Thus, even if K2-106b has no atmosphere, this does not mean that it must have an Earth-like composition. There are still other possibilities. Observations alone cannot rule out all other possibilities, and an improved formation theory is needed to narrow down the possibilities.

To put K2-106 b into perspective, Table 8 and Fig. 8 show all known lmUSPs with radius and mass determination. The dark blue lines in Fig. 8 are the lower and upper limits for planets with Earth-like composition from Hakim et al. (2018). For comparison we also show the classical mass–radius diagram using the models from Zeng et al. (2019) in Fig. 9.

Using the HARDCORE model provided by NASA (Suissa et al. 2018), we also calculate the marginal core radii fraction (CRF). Fig. 10 shows the marginal CRF for all known lmUSPs. The red symbol is K2-106 b. No relation between the marginal core radius fraction and the mass is seen. We also mark the position of the Earth as a blue dot, although the Earth is not a USP.

K2-106 c has the same mass as K2-106 b but a radius of $2.84^{+0.10}_{-0.08}$ $R_\oplus$. This planet thus is likely to have an extended atmosphere. Such planets are often called mini-Neptunes, which is a bit misleading. They are not like Neptune, as their atmospheres contain only a few per cent of the masses of the planets. For example, a Hydrogen-rich atmosphere containing 1–2 per cent of the mass of K2-106 c would fit the data (Zeng et al. 2019). We thus prefer to call such objects C-class planets instead.

The K2-106-system is very interesting, because it contains two planets of almost the same mass but different density. What can we say about the possible formation scenarios? Most of the UPSs in Table 8 are in multiple systems. Because hot Jupiters are lonely, it is unlikely that any of the planets in a system is a remnant core of a gas giant. Since most USPs are either in class-B or class-C there is currently no evidence that they have an unusual composition. Perhaps, they form just like planets at larger distances.

The mass and radius of K2-106 c is $Mp = 7.3^{+2.5}_{-2.4}$ $M_\oplus$ and $Rp = 2.84^{+0.10}_{-0.08}$ $R_\oplus$. The radius thus is significantly larger than that of USPs with similar masses. This planet thus presumably has a hybrid or Hydrogen-rich atmosphere. The fact that one planet has an atmosphere and the other does not can be explained with core-powered mass-loss (Lopez & Fortney 2013; Ginzburg, Schlichting & Sari 2018), or atmospheric evaporation due to the XUV-radiation from the host star (Erkaev et al. 2007; Fossati et al. 2017; Kubyshkina et al. 2018, 2018; Lalitha, Schmitt & Dash 2018; Poppenhaeger, Ketzer & Mallonn 2021). More complicated mechanisms are not needed to explain why the inner planet does not have an extended atmosphere, whereas the outer planet does, even if both planets formed from similar material.

ACKNOWLEDGEMENTS

Based on observations collected at the European Southern Observatory under ESO programme 0103.C-0289(A). We are very thankful to the ESO-staff for carrying out the observations in service mode, and for providing the community with all the necessary tools for reducing and analysing the data.

This paper includes data collected by the Kepler mission and obtained from the MAST data archive at the Space Telescope Science Institute (STScI). Funding for the Kepler mission is provided by the NASA Science Mission Directorate. STScI is operated by the Association of Universities for Research in Astronomy, Inc., under NASA contract NAS 5–26555.

This paper includes data collected by the *TESS* mission. Funding for the *TESS* mission is provided by NASA's Science Mission Directorate. We acknowledge the use of public TOI Release data from pipelines at the *TESS* Science Office and at the *TESS* Science Processing Operations Center.

This work has used data from the European Space Agency (ESA) mission *Gaia* (https://www.cosmos.esa.int/gaia), processed by the *Gaia* Data Processing and Analysis Consortium (DPAC, https://www.cosmos.esa.int/web/gaia/dpac/consortium). Funding for the DPAC has been provided by national institutions, in particular the institutions participating in the *Gaia* Multilateral Agreement. The *Gaia* mission website is https://www.cosmos.esa.int/gaia https://www.cosmos.esa.int/gaia. The *Gaia* archive website is https://archives.esac.esa.int/gaia.

This publication uses data products from the Two Micron All Sky Survey, which is a joint project of the University of Massachusetts and the Infrared Processing and Analysis Center/California Institute of Technology, funded by the National Aeronautics and Space Administration and the National Science Foundation.

This work has used the Mikulski Archive for Space Telescopes (MAST). MAST is a NASA funded project to support and provide to the astronomical community a variety of astronomical data archives, with the primary focus on scientifically related data sets in the optical, ultraviolet, and near-infrared parts of the spectrum.

This research has used the SIMBAD data base, operated at CDS, Strasbourg, France.

Table 8. Properties of USPs with $Mp \leq 25\ M_{\oplus}$ that have mass and radius measurements.

Name	Mass $[M_{\oplus}]$	Radius $[R_{\oplus}]$	Period [d]	a [au]	marginal core radius fraction (CRFmarg) [per cent]	References
TOI-731 b	$0.15^{+0.07}_{-0.04}$	0.59 ± 0.02	0.322	0.0069	52 ± 24	Giacalone et al. (2022)
KOI-4777[2]	$\leq$0.34	0.51 ± 0.03	0.412	0.0069	$<$100	Cañas et al. (2022)
GJ367 b	0.633 ± 0.050	0.699 ± 0.024	0.322	0.0071	95 ± 5	Goffo et al. (2023)
GJ1252 b	1.42 ± 0.18	$1.166^{+0.061}_{-0.058}$	0.548	0.0128	50 ± 21	Serrano et al. (2022)
TOI-500 b	$1.6^{+1.3}_{-0.7}$	1.16 ± 0.12	0.548	0.0128	61 ± 28	Giacalone et al. (2022)
TOI-1442 b	$1.6^{+1.1}_{-0.5}$	1.17 ± 0.06	0.409	0.0071	58 ± 25	Giacalone et al. (2022)
TOI-2290 b	$1.6^{+1.4}_{-0.6}$	1.17 ± 0.07	0.386	0.0086	60 ± 27	Giacalone et al. (2022)
Kepler-78 b	$1.77^{+0.24}_{-0.25}$	$1.228^{+0.019}_{-0.018}$	0.355	0.01	50 ± 20	Dai et al. (2019)
GJ806 b	1.90 ± 0.17	1.331 ± 0.023	0.926	0.0844	35 ± 20	Palle et al. (2023)
TOI-539 b	$1.9^{+1.6}_{-0.7}$	1.25 ± 0.10	0.310	0.0089	56 ± 26	Giacalone et al. (2022)
TOI-833 b	$2.0^{+1.5}_{-0.6}$	1.27 ± 0.07	1.042[a]	0.0171	55 ± 25	Giacalone et al. (2022)
TOI-2445 b	$2.0^{+1.2}_{-0.7}$	1.25 ± 0.08	0.371	0.0064	57 ± 25	Giacalone et al. (2022)
TOI-206 b	$2.2^{+1.4}_{-0.7}$	1.30 ± 0.05	0.736	0.0112	56 ± 24	Giacalone et al. (2022)
TOI-561 b	2.24 ± 0.20	1.31 ± 0.04	1.066[a]	0.0204	51 ± 20	Brinkman et al. (2023)
TOI-1807 b	$2.27^{+0.49}_{-0.58}$	$1.37^{+0.10}_{-0.09}$	0.549	0.0135	46 ± 22	Peng et al. (2022)
LTT3780 b	$2.34^{+0.24}_{-0.23}$	1.35 ± 0.06	0.768	0.0120	48 ± 21	Nowak et al. (2020)
TOI-1263 b	$2.4^{+1.7}_{-0.8}$	1.35 ± 0.06	1.021[a]	0.0185	53 ± 24	Giacalone et al. (2022)
K2-229 b	2.59 ± 0.43	1.165 ± 0.066	0.584	0.0131	79 ± 13	Santerne et al. (2018)
TOI-431 b	3.07 ± 0.35	1.28 ± 0.04	0.490	0.012	72 ± 10	Osborn et al. (2021)
TOI-1685 b	3.43 ± 0.93	1.459 ± 0.065	0.669	0.0116	55 ± 22	Hirano et al. (2021)
TOI-1416 b	3.48 ± 0.47	1.62 ± 0.08	1.067[a]	0.0190	36 ± 20	Deeg et al. (2023)
TOI-2260 b	$3.5^{+2.5}_{-1.3}$	1.62 ± 0.13	0.352	0.0097	40 ± 23	Giacalone et al. (2022)
Kepler-10 b	$3.57^{+0.51}_{-0.53}$	$1.489^{+0.023}_{-0.021}$	0.837	0.0172	51 ± 19	Dai et al. (2019)
TOI-1242 b	$3.7^{+2.9}_{-1.5}$	1.65 ± 0.23	0.381	0.0097	42 ± 26	Giacalone et al. (2022)
TOI-1238 b	$3.76^{+1.15}_{-1.07}$	$1.21^{+0.11}_{-0.10}$	0.764	0.0139	87 ± 18	González-Álvarez et al. (2022)
TOI-1444 b	3.87 ± 0.71	1.397 ± 0.064	0.470	–	69 ± 16	Dai et al. (2021)
TOI-2411 b[b]	$3.9^{+2.8}_{-1.4}$	1.68 ± 0.11	0.783	0.0144	39 ± 22	Giacalone et al. (2022)
TOI-1075 b	$4.0^{+2.7}_{-1.4}$	1.72 ± 0.08	0.604	0.0118	36 ± 21	Giacalone et al. (2022)
CoRoT-7 b	4.73 ± 0.95	1.58 ± 0.10	0.854	0.0172	57 ± 20	Haywood et al. (2014)
TOI-1634 b	$4.91^{+0.68}_{-0.70}$	$1.790^{+0.080}_{-0.081}$	0.989	0.0155	34 ± 19	Cloutier et al. (2021)
HD3167 b	5.02 ± 0.38	$1.70^{+0.18}_{-0.074}$	0.960	0.0186	41 ± 20	Christiansen et al. (2017)
K2-141 b	5.08 ± 0.41	1.51 ± 0.05	0.280	–	67 ± 11	Malavolta et al. (2018)
HD80653 b	5.60 ± 0.43	1.613 ± 0.071	0.720	0.0166	60 ± 17	Frustagli et al. (2020)
Kepler-407 b	6.35 ± 1.4	1.43 ± 0.03	0.669	–	83 ± 11	Marcy et al. (2014)
WASP-47 e	6.83 ± 0.66	1.810 ± 0.027	0.790	0.0173	41 ± 20	Vanderburg et al. (2017)
K2-106 b	$7.80^{+0.71}_{-0.70}$	$1.676^{+0.037}_{-0.037}$	0.571	0.0131	68 ± 9	This article
55 Cnc e	8.59 ± 0.43	1.947 ± 0.038	0.737	0.0154	37 ± 20	Crida et al. (2018)
HD213885 b	$8.83^{+0.66}_{-0.65}$	$1.745^{+0.051}_{-0.052}$	1.008[a]	0.0201	66 ± 10	Espinoza et al. (2020)
TOI-1075 b	$9.95^{+1.36}_{-1.30}$	$1.791^{+0.081}_{-0.116}$	0.605	0.0118	67 ± 16	Essack et al. (2023)
K2-266 b[c]	$11.3^{+11}_{-6.5}$	$3.3^{+1.8}_{-1.3}$	0.658	0.0131	20^{+30}_{-20}	Rodriguez et al. (2018)

Note. Marginal core radius fraction (CRFmarg) (Suissa et al. 2018). Although the mass of this planet has not been determined yet, we include it in the table because the upper limit of the mass is very small. [a]Strictly speaking this planet is not a USP. We also include planets with orbital period between 1.0 and 1.1 d to make sure that we list all USPs even if there is still a small error of the period. [b]TOI-2290 b = TOI-2411 b. [c]This planet has unusually large errors that puts it outside Fig. 8.

This work was generously supported by the Deutsche Forschungsgemeinschaft (DFG) in the framework of the priority programme 'Exploring the Diversity of Extrasolar Planets' (SPP 1992) in program GU 464/22, and by the Thüringer Ministerium für Wirtschaft, Wissenschaft und Digitale Gesellschaft.

EG acknowledges the generous support from the Deutsche Forschungsgemeinschaft (DFG) of the grant HA3279/14-1.

JK gratefully acknowledges the support of the Swedish National Space Agency (SNSA; DNR 2020–00104) and of the Swedish Research Council (VR; Etableringsbidrag 2017–04945).

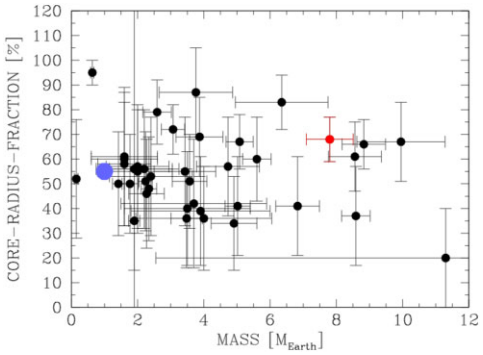

Figure 10. The core-radius fraction versus the mass of the planet. No correlation between the mass of the planet and CRF is seen. The red point is K2-106 b, and the blue point the Earth.

This research is also supported by the European Research Council (ERC) – the European Union's Horizon 2020 research and innovation programme (grant agreement no. 803193/BEBOP). Based on observations made with ESO Telescopes at the La Silla Paranal Observatory under programme 0103.C-0289(A).

DATA AVAILABILITY STATEMENT

The data underlying this article are available in the ESO Science Archive Facility http://archive.eso.org/cms.html and from the Barbara A. Mikulski Archive for Space Telescopes (MAST).

REFERENCES

Adams E. R. et al., 2017, AJ, 153, 82
Adams E. R. et al., 2021, Planet. Sci. J., 2, 152
Adibekyan V. et al., 2022, EPSC Abstracts Vol. 16, EPSC2022-74, Diversity of Terrestrial Planets: A Link to the Chemical Makeup of their Host Stars. Available at: https://doi.org/10.5194/epsc2022-74
Aigrain S., Parviainen H., Pope B. J. S., 2016, MNRAS, 459, 2408
Angelo I., Hu R., 2017, AJ, 154, 232
Armstrong D. J. et al., 2020, Nature, 583, 39
Azevedo Silva T. et al., 2022, A&A, 657, A68
Baranne A. et al., 1996, A&AS, 119, 373
Barnes R., Raymond S. N., Greenberg R., Jackson B., Kaib N. A., 2010, ApJ, 709, L95
Barnes J. R. et al., 2023, MNRAS, 524, 5196
Barragán O., Gandolfi D., Antoniciello G., 2019a, MNRAS, 482, 1017
Barragán O. et al., 2019b, MNRAS, 490, 698
Barragán O., Aigrain S., Rajpaul V. M., Zicher N., 2022a, MNRAS, 509, 866
Barragán O. et al., 2022b, MNRAS, 514, 1606
Barragán O. et al., 2023, MNRAS, 522, 3458
Benbakoura M., Réville V., Brun A. S., Le Poncin-Lafitte C., Mathis S., 2019, A&A, 621, A124
Blanco-Cuaresma S., 2019, MNRAS, 486, 2075
Blanco-Cuaresma S., Soubiran C., Heiter U., Jofré P., 2014, A&A, 569, A111
Bolmont E., Breton S. N., Tobie G., Dumoulin C., Mathis S., Grasset O., 2020, A&A, 644, A165
Bonomo A. S. et al., 2019, Nat. Astron., 3, 416
Bonomo A. S. et al., 2023, A&A, 677, A33
Bower D. J., Hakim K., Sossi P. A., Sanan P., 2022, Planet. Sci. J., 3, 93
Brandner W., Calissendorff P., Frankel N., Cantalloube F., 2022, MNRAS, 513, 661
Brinkman C. et al., 2023, AJ, 165, 88
Briot D., Schneider J., 2010, in Coudé du Foresto V., Gelino D. M., Ribas I., eds, ASP Conf. Ser. Vol. 430, Pathways Towards Habitable Planets. Astron. Soc. Pac., San Francisco, p. 409
Brott I., Hauschildt P. H., 2005, in Turon C., O'Flaherty K. S., Perryman M. A. C., eds, ESA SP-576: The Three-Dimensional Universe with Gaia. ESA, Noordwijk, p. 565
Bruntt H. et al., 2010, MNRAS, 405, 1907
Cañas C. I. et al., 2022, AJ, 163, 3
Castelli F., Kurucz R. L., 1993, VizieR Online Data Catalog, J/A + A/281/817
Choi J., Dotter A., Conroy C., Cantiello M., Paxton B., Johnson B. D., 2016, ApJ, 823, 102
Christiansen J. L. et al., 2017, AJ, 154, 122
Cloutier R. et al., 2021, AJ, 162, 79
Crida A., Ligi R., Dorn C., Borsa F., Lebreton Y., 2018, Res. Notes Am. Astron. Soc., 2, 172
da Silva L. et al., 2006, A&A, 458, 609
Dai F., Masuda K., Winn J. N., Zeng L., 2019, ApJ, 883, 79
Dai F. et al., 2021, AJ, 162, 62
Damasso M. et al., 2018, A&A, 615, A69
Deeg H. J. et al., 2023, A&A, 677, A12
Diamond-Lowe H. et al., 2022, AJ, 164, 172
Dorn C., Harrison J. H. D., Bonsor A., Hands T. O., 2019, MNRAS, 484, 712
Dotter A., 2016, ApJS, 222, 8
Doyle A. P., Davies G. R., Smalley B., Chaplin W. J., Elsworth Y., 2014, MNRAS, 444, 3592
Eastman J., Gaudi B. S., Agol E., 2013, PASP, 125, 83
Elkins-Tanton L. T., 2008, Earth Planet. Sci. Lett., 271, 181
Erkaev N. V., Kulikov Y. N., Lammer H., Selsis F., Langmayr D., Jaritz G. F., Biernat H. K., 2007, A&A, 472, 329
Espinoza N. et al., 2020, MNRAS, 491, 2982
Essack Z. et al., 2023, AJ, 165, 47
Esteves L. J., de Mooij E. J. W., Jayawardhana R., Watson C., de Kok R., 2017, AJ, 153, 268
Feroz F., Hobson M. P., 2008, MNRAS, 384, 449
Feroz F., Hobson M. P., Bridges M., 2009, MNRAS, 398, 1601
Feroz F., Hobson M. P., Cameron E., Pettitt A. N., 2019, Open J. Astrophys., 2, 10
Fossati L. et al., 2017, A&A, 598, A90
Fridlund M. et al., 2020, MNRAS, 498, 4503
Frustagli G. et al., 2020, A&A, 633, A133
Gaia Collaboration, 2021, A&A, 649, A1
García Muñoz A., Fossati L., Youngblood A., Nettelmann N., Gandolfi D., Cabrera J., Rauer H., 2021, ApJ, 907, L36
Gelman A., Rubin D. B., 1992, Stat. Sci., 7, 457
Gelman A., Carlin J. B., Stern H. S., Rubin D. B., 2004, Bayesian Data Analysis. Chapman & Hall/CRC Press
Georgieva I. Y. et al., 2021, MNRAS, 505, 4684
Georgieva I. Y. et al., 2023, A&A, 674, A117
Giacalone S. et al., 2022, AJ, 163, 99
Ginzburg S., Schlichting H. E., Sari R., 2018, MNRAS, 476, 759
Goffo E. et al., 2023, ApJ, 955, L3
González-Álvarez E. et al., 2022, A&A, 658, A138
Grayver A., Bower D. J., Saur J., Dorn C., Morris B. M., 2022, ApJ, 941, L7
Guenther E. W. et al., 2012, A&A, 537, A136
Guenther E. W. et al., 2017, A&A, 608, A93
Guenther E. W., Wöckel D., Chaturvedi P., Kumar V., Srivastava M. K., Muheki P., 2021, MNRAS, 507, 2103
Guo S.-S., 2023, Res. Astron. Astrophys., 23, 095014
Hakim K., Rivoldini A., Van Hoolst T., Cottenier S., Jaeken J., Chust T., Steinle-Neumann G., 2018, Icarus, 313, 61
Haswell C. A. et al., 2012, ApJ, 760, 79
Haywood R. D. et al., 2014, MNRAS, 443, 2517
Hebb L. et al., 2010, ApJ, 708, 224
Hellier C. et al., 2009, Nature, 460, 1098
Hirano T. et al., 2021, AJ, 162, 161
Ilic N., Poppenhaeger K., Hosseini S. M., 2022, MNRAS, 513, 4380
Ito Y., Ikoma M., Kawahara H., Nagahara H., Kawashima Y., Nakamoto T., 2015, ApJ, 801, 144
Kipping D. M., 2010, MNRAS, 408, 1758
Kislyakova K. G. et al., 2017, Nat. Astron., 1, 878

Kosiarek M. R. et al., 2019, AJ, 157, 97
Kubyshkina D. et al., 2018, A&A, 619, A151
Kurucz R. L., 1993, VizieR Online Data Catalog, p. VI/39
Kurucz R. L., 2005, Mem. Soc. Astron. Ital. Suppl., 8, 14
Kurucz R. L., 2013, Astrophysics Source Code Library, record ascl:1303.024
Lalitha S., Schmitt J. H. M. M., Dash S., 2018, MNRAS, 477, 808
Lam K. W. F. et al., 2021, Science, 374, 1271
Lam K. W. F. et al., 2023, MNRAS, 519, 1437
Lanza A. F., 2021, A&A, 653, A112
Léger A. et al., 2009, A&A, 506, 287
Leleu A. et al., 2022, preprint (arXiv:2207.07456)
Ligi R. et al., 2019, A&A, 631, A92
Livingston J. H. et al., 2018, AJ, 156, 277
Lopez E. D., Fortney J. J., 2013, ApJ, 776, 2
Malavolta L. et al., 2018, AJ, 155, 107
Maldonado J. et al., 2022, A&A, 663, A142
Mamajek E. E., Hillenbrand L. A., 2008, ApJ, 687, 1264
Marcy G. W. et al., 2014, ApJS, 210, 20
McCormac J. et al., 2020, MNRAS, 493, 126
Mocquet A., Grasset O., Sotin C., 2014, Phil. Trans. R. Soc. A, 372, 20130164
Morton T. D., 2015, Astrophysics Source Code Library, record ascl:1503.010
Motalebi F. et al., 2015, A&A, 584, A72
Mura A. et al., 2011, Icarus, 211, 1
Nowak G. et al., 2020, A&A, 642, A173
Osborn A. et al., 2021, MNRAS, 507, 2782
Osborn A. et al., 2023, MNRAS, 526, 548
Osborne H. L. M. et al., 2023, MNRAS
Otegi J. F., Bouchy F., Helled R., 2020, A&A, 634, A43
Palle E. et al., 2023, A&A, 678, A80
Pecaut M. J., Mamajek E. E., Bubar E. J., 2012, ApJ, 746, 154
Peng P., Xiong H., Li H., Li F., Wang T., 2022, preprint (arXiv:2210.04162)
Pepe F. et al., 2014, Astron. Nachr., 335, 8
Pepe F. et al., 2021, A&A, 645, A96
Persson C. M. et al., 2022, A&A, 666, A184
Petrovich C., Deibert E., Wu Y., 2019, AJ, 157, 180
Plotnykov M., Valencia D., 2020, MNRAS, 499, 932
Poppenhaeger K., Ketzer L., Mallonn M., 2021, MNRAS, 500, 4560
Rappaport S., Sanchis-Ojeda R., Rogers L. A., Levine A., Winn J. N., 2013, ApJ, 773, L15
Reinhardt C., Meier T., Stadel J., Otegi J., Helled R., 2022, MNRAS, 517, 3132
Ridden-Harper A. R. et al., 2016, A&A, 593, A129
Rodrigues T. S. et al., 2014, MNRAS, 445, 2758
Rodrigues T. S. et al., 2017, MNRAS, 467, 1433
Rodríguez Martínez R. et al., 2023, AJ, 165, 97
Rodriguez J. E. et al., 2018, AJ, 156, 245
Rouan D., Deeg H. J., Demangeon O., Samuel B., Cavarroc C., Fegley B., Léger A., 2011, ApJ, 741, L30
Sandford E., Kipping D., 2017, AJ, 154, 228
Santerne A. et al., 2018, Nat. Astron., 2, 393
Sbordone L., Bonifacio P., Castelli F., Kurucz R. L., 2004, Mem. Soc. Astron. Ital. Suppl., 5, 93
Scora J., Valencia D., Morbidelli A., Jacobson S., 2020, MNRAS, 493, 4910
Serrano L. M. et al., 2022, Nat. Astron., 6, 736
Singh V., Bonomo A. S., Scandariato G., Cibrario N., Barbato D., Fossati L., Pagano I., Sozzetti A., 2022, A&A, 658, A132
Sinukoff E. et al., 2017, AJ, 153, 271
Skrutskie M. F. et al., 2006, AJ, 131, 1163
Smith A. M. S. et al., 2018, MNRAS, 474, 5523
Smith A. M. S. et al., 2019, Acta Astron., 69, 135
Staab D. et al., 2020, Nat. Astron., 4, 399
Stassun K. G. et al., 2018, AJ, 156, 102
Suissa G., Chen J., Kipping D., 2018, MNRAS, 476, 2613
Tabernero H. M. et al., 2020, MNRAS, 498, 4222
Tian M., Heng K., 2023, ApJ, preprint (arXiv:2301.10217)
Tsiaras A. et al., 2016, ApJ, 820, 99
Uzsoy A. S. M., Rogers L. A., Price E. M., 2021, ApJ, 919, 26
Vanderburg A., Johnson J. A., 2014, PASP, 126, 948
Vanderburg A. et al., 2017, AJ, 154, 237
Vines J. I., Jenkins J. S., 2022, MNRAS, 513, 2719
Vogt S. S. et al., 2015, ApJ, 814, 12
Wagner F. W., Sohl F., Hussmann H., Grott M., Rauer H., 2011, Icarus, 214, 366
Zeng L. et al., 2019, Proc. Natl. Acad. Sci., 116, 9723
Zieba S. et al., 2022, A&A, 664, A79
Zilinskas M., van Buchem C. P. A., Miguel Y., Louca A., Lupu R., Zieba S., van Westrenen W., 2022, A&A, 661, A126

SUPPORTING INFORMATION

Supplementary data are available at *MNRAS* online.

suppl_data

Please note: Oxford University Press is not responsible for the content or functionality of any supporting materials supplied by the authors. Any queries (other than missing material) should be directed to the corresponding author for the article.

APPENDIX: POSTERIOR PARAMETERS

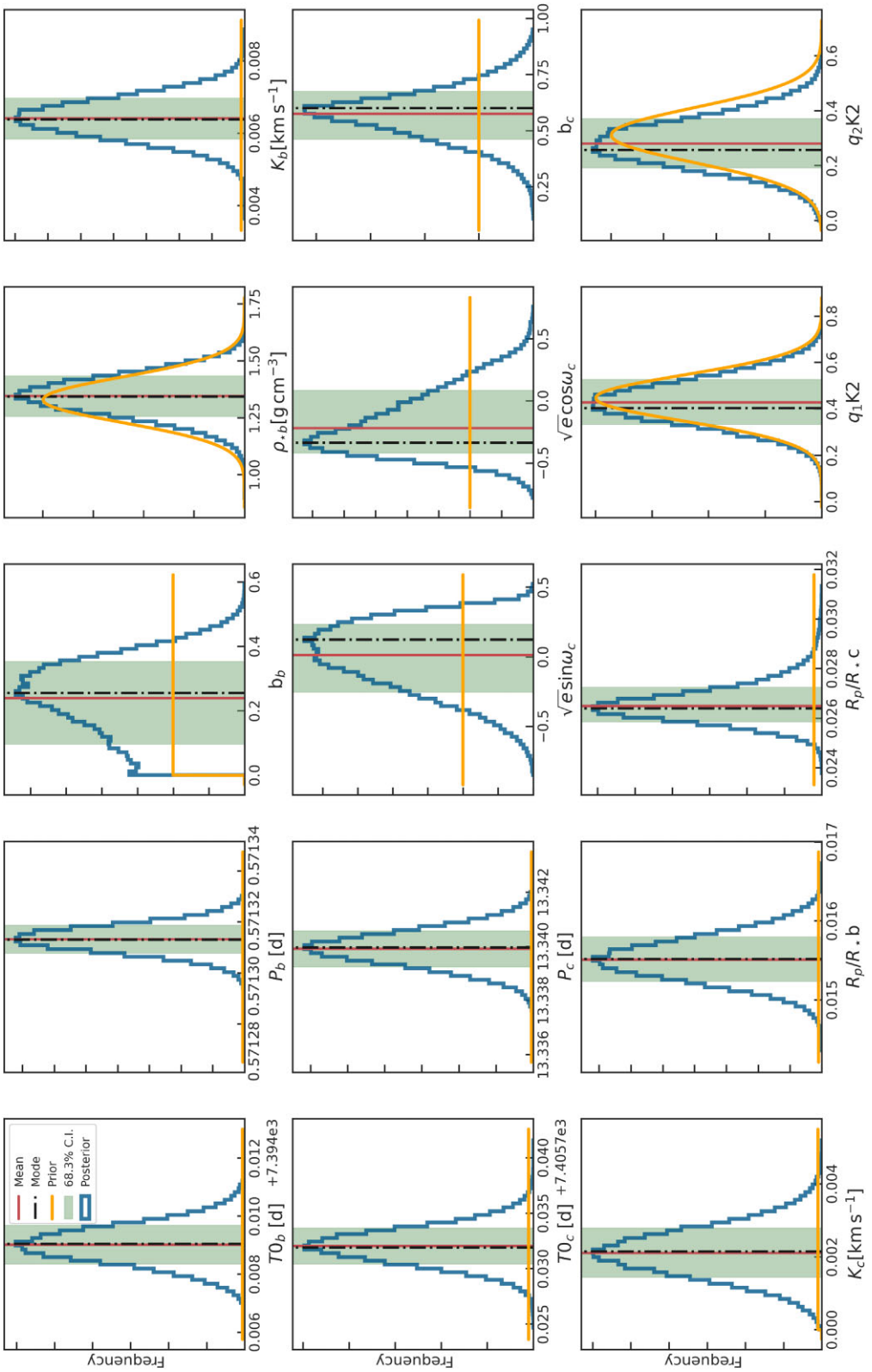

Figure A1. Posterior distributions of the fitted parameters for the best-fitting model discussed in Section 2.6.

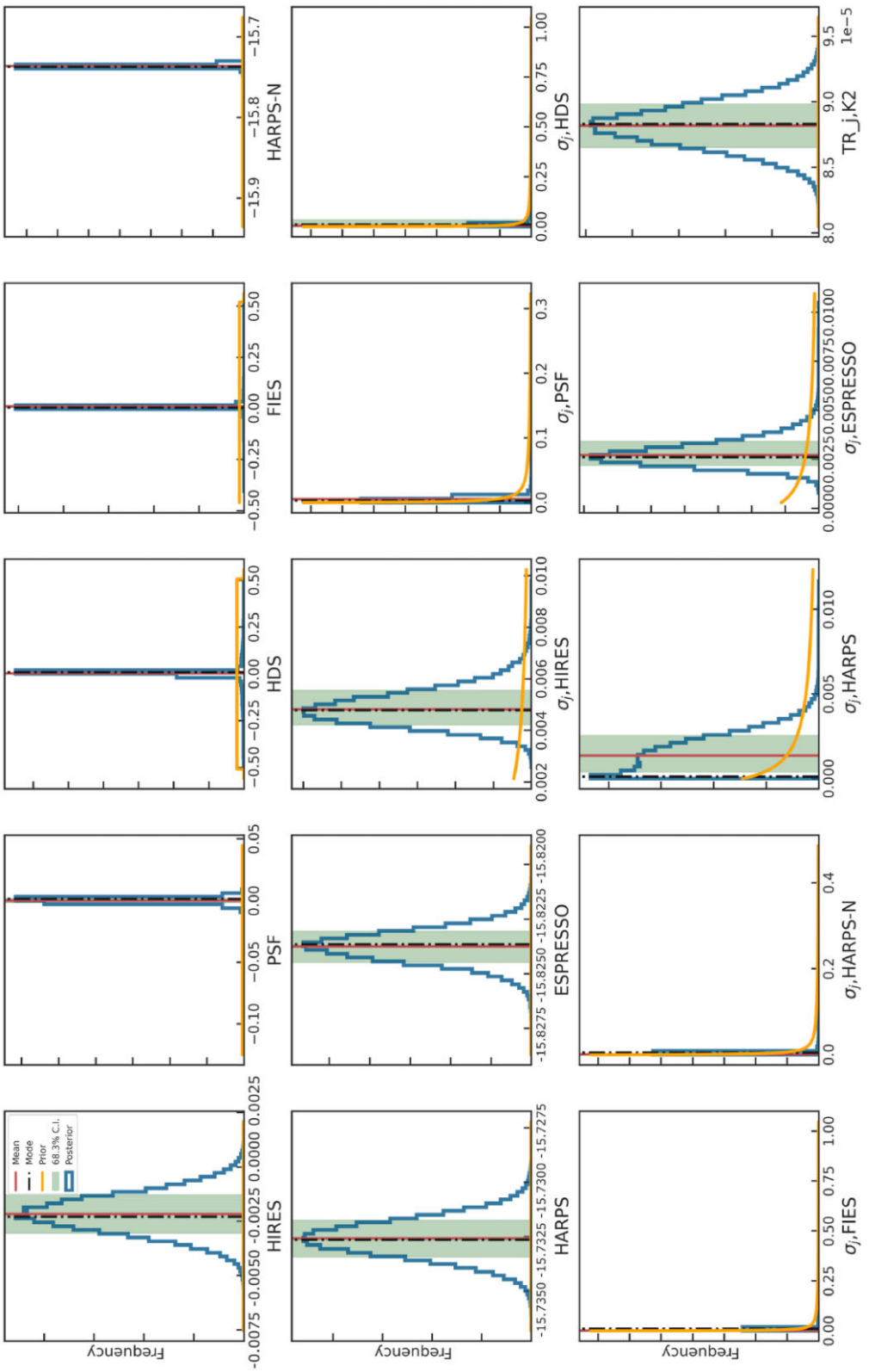

Figure A2 – *continued*.

This paper has been typeset from a TEX/LATEX file prepared by the author.